nature communications

Article

https://doi.org/10.1038/s41467-026-70252-2

Ballistic transport in nanodevices based on single-crystalline Cu thin films

Received: 14 April 2025

Accepted: 18 February 2026

Published online: 07 March 2026

Yongjin Cho[1], Su Jae Kim[2], Min-Hyoung Jung[3], Yousil Lee[4], Hu Young Jeong[5], Young-Min Kim[3], Hu-Jong Lee[1], Seong-Gon Kim[6] ✉, Se-Young Jeong[7,8] ✉ & Gil-Ho Lee[1,9] ✉

In ballistic transport, the movement of charged carriers remains unimpeded by scattering events. In this limit, microscopic parameters such as crystal momentum, spin and quantum phase are well conserved, allowing electrons to maintain their quantum coherence over longer distances. Nanoscale materials, such as carbon nanotubes, graphene, and nanowires, can exhibit ballistic transport. However, their scalability in devices is significantly limited. While deposited metal films offer scalability for nanodevices, their short electronic mean free paths hinder ballistic transport. In this study, we investigated the electronic transport in cross-geometry devices fabricated with 90-nm-thick Cu films without grain boundaries. We demonstrated ballistic transport in devices with channel widths of 150 nm at temperatures below 85 K via negative bend resistance measurements. Our findings establish a scalable platform for exploring the intrinsic quantum mechanical properties of Cu, advancing both the fundamental understanding of quantum transport in metals and its practical applications in next-generation electronic quantum technologies.

When the electronic mean free path exceeds the device size, electrons undergo ballistic transport within the device, experiencing minimal scattering. Ballistic transport can reveal intrinsic quantum properties of solid-state materials, as electrons' quantum information—such as crystal momentum, spin, and quantum phase—is well conserved[1–4]. Research on quantum properties of normal metals, including electronic band structure, Fermi surface topology, conductivity, and magnetoresistance, has accelerated in recent years[5–12]. Cu is used in electronic circuits owing to its conductivity, reliability, and versatility. It remains crucial in the electronics industry, used for high-speed data-processing cables and interconnects in advanced semiconductor devices. Electronic band structure, Fermi surface topology, and Fermi velocity of bulk Cu are well understood through various measurements[13–19]. However, growing atomically flat and uniform Cu thin films without grain boundaries (GBs) has been technically challenging, and in-plane ballistic transport in Cu thin film nanostructures has not been achieved, limiting the exploitation of their intrinsic quantum properties. Although polycrystalline Cu thin films prepared by sputtering and post-annealing have shown low room-temperature resistivities[20] ($2.0–2.2 \times 10^{-8}$ Ω·m), ballistic transport was not explicitly examined.

In this study, we demonstrated ballistic transport in nanoscale devices composed of atomically flat single-crystalline Cu(111) thin films (SCCFs) (Supplementary Fig. 1) grown using the atomic sputtering

[1]Department of Physics, Pohang University of Science and Technology, Pohang, Republic of Korea. [2]Crystal Bank Research Institute, Pusan National University, Busan, Republic of Korea. [3]Department of Energy Science, Sungkyunkwan University, Suwon, Republic of Korea. [4]Copper Innovative Technology (CIT) Co. Ltd., Busan, Republic of Korea. [5]Graduate School of Semiconductor Materials and Devices Engineering, Ulsan National Institute of Science and Technology, Ulsan, Republic of Korea. [6]Department of Physics and Astronomy, Mississippi State University, Mississippi State, MS, USA. [7]Department of Physics, Korea Advanced Institute of Science and Technology (KAIST), Daejeon, Republic of Korea. [8]Department of Optics and Mechatronics Engineering, Engineering Research Center for Color-Modulated Extra-Sensory Perception Technology, Pusan National University, Busan, Republic of Korea. [9]Asia Pacific Center for Theoretical Physics, Pohang, Republic of Korea. ✉e-mail: sk162@msstate.edu; sjeong9@kaist.ac.kr; lghman@postech.ac.kr

epitaxy (ASE) technique[21]. This method addresses challenges in conventional metal-film deposition, such as surface oxidation and electrical performance degradation due to defects such as GBs and impurities[22]. We observed negative bend resistance in cross-geometry devices, indicating ballistic transport[23]. The electronic mean free path of the 80-nm-thick SCCF was 150 nm at a temperature below 85 K (Supplementary Fig. 2). Our SCCF enables studies on the quantum nature of Cu thin films, including topological properties[24–26] and phase-coherent quantum interference[27,28]. It also suggests potential applications in quantum circuits, spintronic devices, and Cu interconnect technology[29–31].

Results

Ballistic transport in SCCFs

Using standard electron beam lithography and argon-ion etching, Hall-bar-shaped devices with nominal channel widths (W) of 10 µm, 1 µm, 250 nm, and 150 nm were fabricated with a thickness (t) of ~90 nm (Fig. 1a, b and Supplementary Fig. 3). Here, W denotes the nominal channel width, which may differ from the actual one. In all devices measured, the actual channel width deviated by no more than ~10% from the designed width. Cross-sectional transmission electron microscopy (TEM) images revealed perfectly aligned Cu atoms, with 2.07 Å spacings, in the [111] direction of the thin film (Fig. 1b), indicating that the thin film

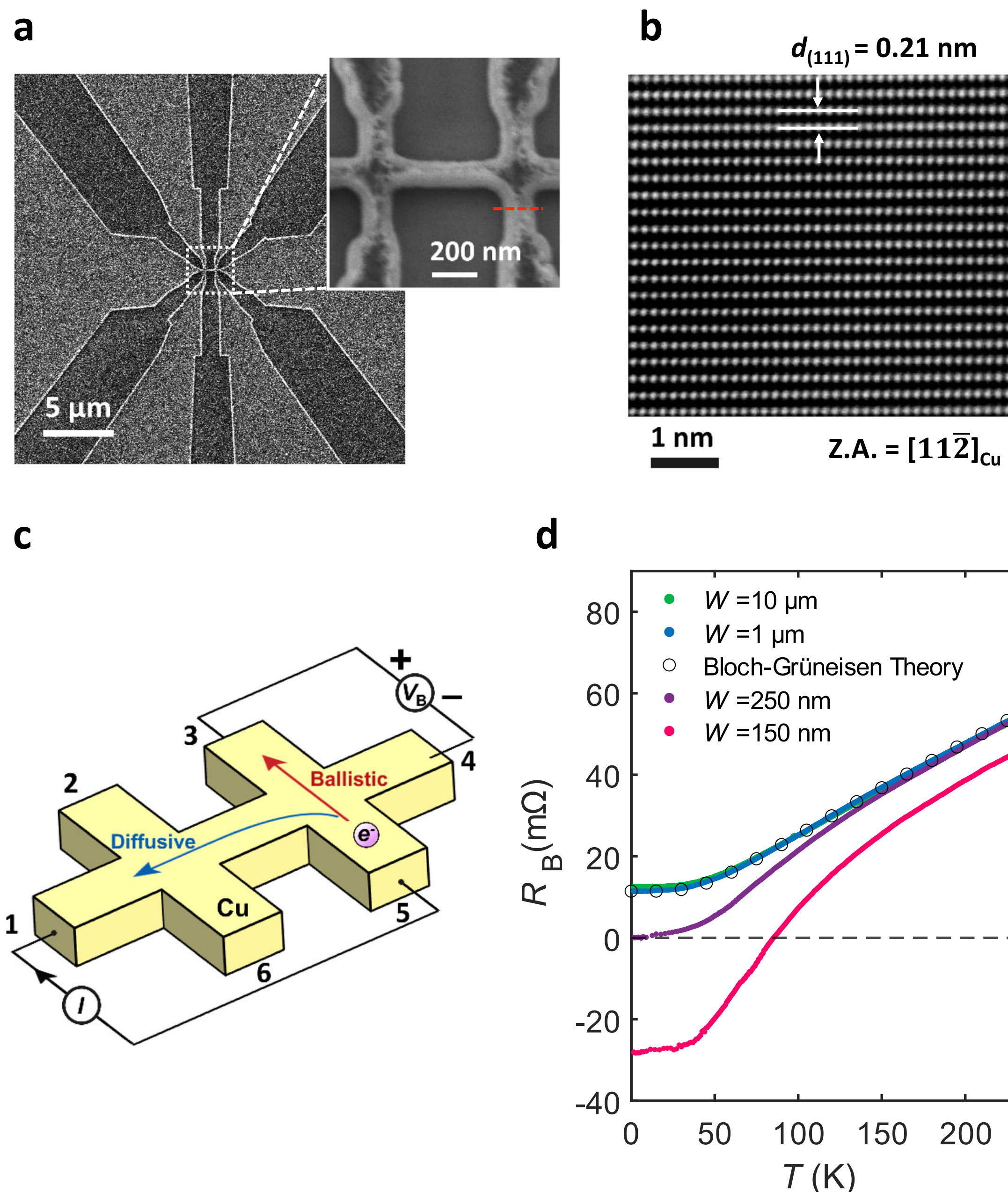

Fig. 1 | Ballistic transport in single-crystalline Cu(111) thin film (SCCF). **a** Scanning electron microscope (SEM) image of a Hall bar device with a nominal channel width (W) of 150 nm. The inset illustrates the enlarged SEM image of the marked area in (**a**). The red line indicates the position where the cross-sectional transmission electron microscopy (TEM) sample was prepared using focused ion beam milling. **b** TEM image showing the cross-sectional view of the Hall bar device, prepared using focused ion beam milling along the red line indicated in the inset of (**a**). Electron beam was aligned along the $[11\bar{2}]$ zone axis (Z.A.) of Cu. **c** Schematic representation of the bend-resistance (R_B) measurement. Electron trajectories for diffusive and ballistic transport are indicated by blue and red arrows, respectively. **d** Temperature (T) dependence of R_B in Hall bars with W = 10 µm, 1 µm, 250 nm, and 150 nm. Circle symbols depict the fitting of R_B with W = 1 µm and 10 µm using the Bloch–Grüneisen function.

retained its high crystalline quality after fabrication (Supplementary Fig. 4). The bend resistance ($R_B = V_B/I$) was measured in the cross configuration (Fig. 1c), with current (I) injected from terminal 1 to terminal 5, and bend voltage (V_B) was measured between terminals 3 and 4. In a diffusive transport regime, where the electronic mean free path (l_{mfp}) is shorter than the device length, the van der Pauw formula $R_B = (\rho \ln 2)/(t\pi)$ for symmetric cross geometry can be applied. In this regime, R_B is expected to be positive[32] as the resistivity (ρ) is inherently positive. The temperature (T) dependence of ρ in diffusive metals is predominantly influenced by electron–acoustic phonon scattering, which follows the Bloch–Grüneisen formula (Eq. (1)) derived from the Boltzmann transport theory[33,34].

$$\rho(T) = \rho_0 + \alpha_{el-ph}\left(\frac{T}{\Theta_R}\right)^5 \int_0^{\Theta_R/T} \frac{x^5}{(e^x - 1)(1 - e^{-x})} dx \quad (1)$$

Here, ρ_0 represents the residual resistivity due to temperature-independent scattering by defects such as GBs and impurities, $\alpha_{el\text{-}ph}$ represents the electron–phonon coupling strength, and Θ_R is the Debye temperature. As shown in Fig. 1d, the temperature dependence of R_B for devices with $W = 10$ and 1 µm can be well fitted[35] with Eq. (1) using fitting parameters $\alpha_{el\text{-}ph} = 8.8 \times 10^{-8}\ \Omega$m and $\Theta_R = 270$ K, indicative of the occurrence of diffusive transport over the entire temperature range. The fitting parameters $\alpha_{el\text{-}ph}$ and Θ_R were determined from the fitting analysis (Supplementary Fig. 5). We also note that Hall measurements of a device with $W = 10$ µm (Supplementary Fig. 6) indicate the presence of multiple carrier types at 1.7 K, but an electron-like band provides the dominant contribution to the conductance (Supplementary Fig. 7 and Supplementary Table 1). These results support the use of Eq. (1) as an effective single-carrier Bloch–Grüneisen description of $R_B(T)$. The sample used in this study is nearly single-crystalline and would typically be expected to exhibit a Debye temperature close to or even higher than that of polycrystalline Cu. However, the observed Debye temperature of 270 K is slightly lower than the commonly reported bulk value (~330 K). We attribute this deviation to the thin film geometry and the fabrication process. In particular, device fabrication steps such as Ar-ion etching and chemical treatments may introduce surface roughening, partial oxidation, or other structural imperfections that alter the phonon spectrum and reduce the effective Debye temperature. Similar reductions in Debye temperature due to dimensional confinement and surface degradation have also been reported in sputtered Cu thin films[36]. Indeed, $R_B(T)$ of the device with $W = 10$ µm remains positive and is well described by the Bloch–Grüneisen formula, consistent with fully diffusive transport in a device $W \gg l_{mfp}$. However, $R_B(T)$ of devices with $W \le 250$ nm, which is comparable to or shorter than l_{mfp}, deviates from the value expected from the Bloch–Grüneisen formula. For the device with $W = 150$ nm, R_B even shows negative values below 85 K. Although decreasing W increases the contribution of edge scattering and thus reduces l_{mfp} (Supplementary Fig. 8), l_{mfp} nonetheless exceeds $W = 150$ nm and ballistic transport persists. We also estimated the mean free path $l_{mfp,Drude} \approx 42$ nm using Drude model Eq. (2):

$$l_{mfp,\,Drude} = \frac{m^* v_F}{ne^2\rho} \quad (2)$$

Here, we used the measured resistivity $\rho = 1.03 \times 10^{-8}\ \Omega$m in the device of $W = 150$ nm and the carrier density $n = 1.683 \times 10^{29}\ m^{-3}$ extracted from the Hall analysis at 1.7 K (Supplementary Fig. 9). A Fermi velocity[37] $v_F = 1.57 \times 10^6$ m/s and an effective mass[38] $m^* = 1.1843 \times 10^{-30}$ kg from the bulk Cu were used. $l_{mfp,Drude}$ is slightly different from the experimentally inferred l_{mfp} (~150 nm at 1.7 K) from the observation of negative R_B in the device of $W = 150$ nm. The difference may be attributed to the fact that the electric parameters of the 90-nm-thick, 150-nm-wide Cu device can differ from those of bulk Cu.

Counter-intuitive negative bend resistance has been observed in high-mobility two-dimensional (2D) electronic systems such as GaAs/AlGaAs heterostructures and graphene[3,4,39] owing to ballistic transport[40], but not in deposited metallic films. In the ballistic regime, electrons from terminal 5 can propagate to terminal 3 without scattering, as shown by the red arrow in Fig. 1c. As electrons accumulate near terminal 3, a negative electrical potential builds up, decreasing R_B, which becomes negative[23]. These findings confirm that ballistic transport, previously hidden by electron scattering at GBs, emerges in an SCCF when GBs are eliminated[41]. To verify that the observed negative R_B is not due to a specific choice of current–voltage configuration or artifact, we performed additional measurements across all contact configurations (Supplementary Fig. 10 and Supplementary Table 2). At high temperatures, the R_B of the device with $W = 150$ nm appears slightly lower than that of the other devices with larger W. This difference may arise from geometric imperfections introduced during fabrication, as supported by simulations in Supplementary Fig. 11.

Structural defects in the SCCF and a polycrystalline Cu thin film (PCCF)

We analyzed the crystallographic microstructure of the SCCF, as high crystalline quality is essential for ballistic transport. During thin-film growth, GBs and twin boundaries (TBs) form owing to lattice mismatch with the substrate. While TBs are unavoidable, the formation of GBs can be suppressed using a growth technique that considers extended atomic distance mismatch (EADM)[22]. The distribution of GBs and TBs was analyzed for a polycrystalline Cu thin film (PCCF; Fig. 2a–c), an SCCF with minimal GBs (Fig. 2d–f), and an SCCF without GBs (Fig. 2g–i) using misorientation line mapping, electron backscatter diffraction (EBSD), and SEM[42,43]. GBs and TBs are denoted by blue and red lines, respectively, in Fig. 2. PCCF usually contains both GBs and TBs (enlarged misorientation maps of the boxed areas in a, d, and g left panels are shown in the right upper panels, and those of the boxed areas in the upper panels are shown in the right lower panels). As shown in Fig. 2a, the PCCF has many grains (a conventional PCCF is expected to have trillions of grains on the two-inch wafer[44] and each grain has a different orientation, as illustrated by the numbered indicators in the right lower panel of Fig. 2a). The Cu thin films grown by ASE show perfect alignment along the (111) plane (Fig. 2e) despite the presence of some GBs (Fig. 2d). The GBs observed in the misorientation line map in Fig. 2d are close to the TBs; thus, they do not appear as different grains in the EBSD map, as they deviate slightly from the ideal TB condition of 60° (deviation of 1°–2°)[45]. These GBs can influence electronic transport, and thus, we used only the SCCF without GBs in this study. A well-grown SCCF (Fig. 2g) is devoid of GBs, contains only TBs, and exhibits two orientations, I and II (Fig. 2i, right lower panel). The crystallographic orientation of the SCCF follows either ABC… or ACB… stacking, satisfying symmetry operation by 60° rotation (Supplementary Fig. 12). Although the TB density fluctuates across areas, it remains within the same order of magnitude. Unlike GBs, TBs minimally affect electrical resistivity because: (1) charged defects do not form around TBs, resulting in negligible potential variation near TB[46,47], and (2) well-matched Fermi surfaces of adjacent grains on either side of a TB reduce electron wave scattering, as the Fermi surface of Cu remains unchanged with 60° rotation about the (111) axis[33,45,47–49].

GB dependence of electrical transport

Figure 3 shows the electronic transport behavior for different GB lengths. L_{GB}, defined as the total length of line segments separating the grains in the misorientation line maps, was measured over an area of 7.7 µm × 22.7 µm using the EBSD technique (Supplementary Fig. 12)[42,43]. More GBs generally increase resistivity by acting as scattering sites for electrons. Thus, as the grain size (d) decreases, i.e., as L_{GB} increases, the resistivity contribution of the GBs increases. According to the Mayadas–Shatzkes (MS) model (Eq. 3), which

https://doi.org/10.1038/s41467-026-70252-2

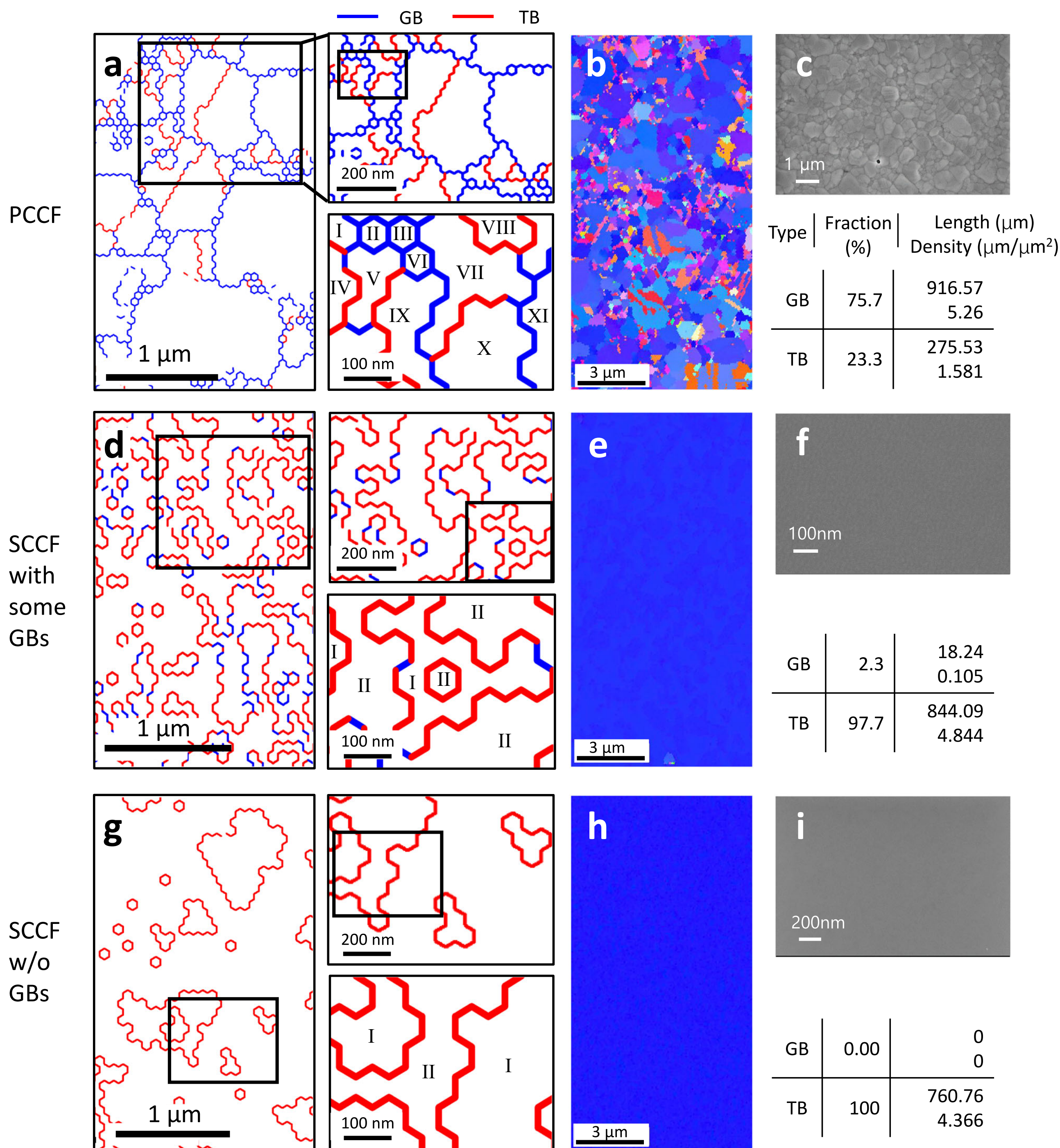

Fig. 2 | Grain boundaries (GBs) and twin boundaries (TBs) in the polycrystalline Cu thin film (PCCF) and single-crystalline Cu(111) thin film (SCCF).
a Misorientation line map of the PCCF and enlarged images of the marked area in each map. GBs and TBs are depicted by blue and red lines, respectively. For PCCF, misorientation-line distributions indicate the presence of both TBs and GBs. The Roman numerals in the bottom right panel represent the orientations of each grain. In the 2-inch wafer-sized PCCF, there are approximately trillions(10^{12}) of different orientations[44]. **b** Electron backscatter diffraction (EBSD) map of the PCCF showing random alignment. **c** Scanning electron microscope (SEM) image of the PCCF showing rough surface and GBs. **d** Misorientation line map of the SCCF with reduced number of GBs and enlarged images of the marked areas in each map. **e** EBSD map of (**d**) sample showing perfect alignment along the (111) plane. **f** SEM image of (**d**) showing a high-quality surface and absence of GBs. **g** Misorientation line map of an SCCF without GBs and enlarged images of the marked area in each map. The Roman numerals in the bottom right panel represent the orientations of each grain. In the two-inch wafer-sized SCCF, there are only two different orientations, which are stacked along ABC… and ACB… respectively. **h** EBSD map of (**g**) sample showing perfect alignment along the (111) plane. **i** SEM image of (**g**) showing high-quality surface and no trace of GBs. Right upper panels of (**a**, **d**, **g**) are enlarged images of boxed area of left panels, and right lower panels are enlarged images of boxed area of upper panels, respectively. Tables on the right of (**b**, **e**, **h**) give the fraction of GB and TB, and their density in the length (nm/µm²) of each sample.

https://doi.org/10.1038/s41467-026-70252-2

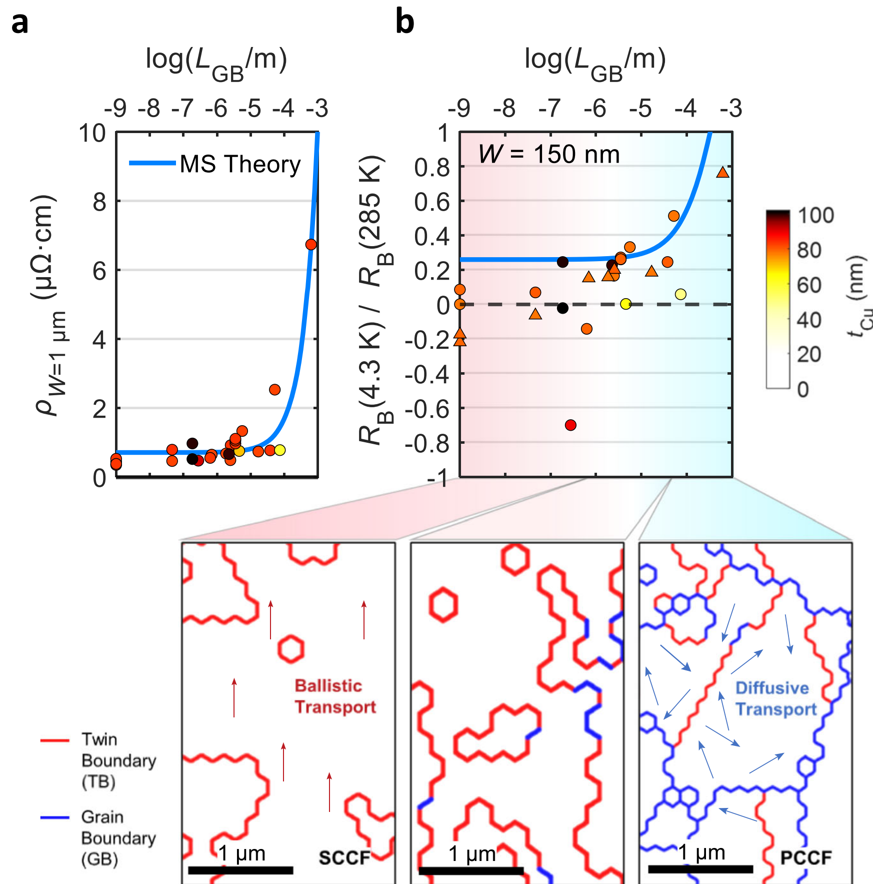

Fig. 3 | GB dependence of electrical transport. a Longitudinal resistivity measured at 4.3 K as a function of GB length L_{GB} for the device of width $W = 1\ \mu m$. Blue solid line represents the Mayadas–Shatzkes (MS) theory fit. **b** Normalized bend resistance R_B as a function of L_{GB} for $W = 150$ nm. Blue solid line represents the MS theory fit from (**a**) circles and triangles represent the device without and with annealing processes, respectively. Color of the symbols represents the thickness, t_{Cu}. Bottom panels represent misorientation line maps of the single-crystalline Cu(111) thin film (SCCF) without GBs (left), SCCF with some GBs (middle), and polycrystalline Cu thin film (PCCF) (right).

quantitatively describes electron scattering at GBs[50–52], the resistivity decreases as the grain size (d) increases, whereas it increases with the probability of electron scattering at the GBs (S):

$$\frac{\rho_g}{\rho_i} = \left\{3\left[\frac{1}{3} - \frac{1}{2}\alpha + \alpha^2 - \alpha^3 \ln\left(1 + \frac{1}{\alpha}\right)\right]\right\}^{-1} \quad (3a)$$

$$\alpha = \frac{l_{mfp}}{d}\frac{S}{1 - S} \quad (3b)$$

Here, ρ_g represents the resistivity arising from electron scattering at the GBs, while ρ_i denotes the intrinsic resistivity from all other sources excluding GBs. As shown in Fig. 3a, L_{GB} dependence of the resistivity of the device with $W = 1\ \mu m$ at 4.3 K, which is in the diffusive regime, is well fitted by the MS relationship $d \propto (L_{GB})^{-1}$ for a 2D system. Figure 3b shows L_{GB} dependence of R_B at 4.3 K normalized with that at 285 K for devices with $W = 150$ nm. As shown in Supplementary Fig. 13, for devices with $W = 1\ \mu m$, the normalized R_B shows similar L_{GB} dependence of resistivity as the film is in a diffusive regime for all L_{GB} values. By contrast, for devices with $W = 250$ nm (Supplementary Fig. 13) and 150 nm, the MS model cannot explain the normalized R_B for small values of L_{GB}, where l_{mfp} exceeds W, and R_B becomes negative.

Geometrical effect on the transport measurement for SCCF

To further investigate the ballistic transport behavior under a magnetic field, we investigated the magnetic field dependence of the bend resistance R_B (Fig. 4). We symmetrized R_B to suppress intermixed signals from slight asymmetries and misalignments between contacts. A magnetic field B was applied normal to the SCCF, which was parallel to the (111) direction. As the magnitude of $|B|$ increased, the symmetrized bend resistance R_B^s gradually increased, because electron deflection due to the Lorentz force caused fewer electrons to reach the opposite terminal 3 (Fig. 4a)[40]. This ballistic transport behavior can be qualitatively explained using the Landauer–Büttiker approach[23]. R_B^s for a single channel can be expressed in terms of the forward mode-averaged transmission probability P_{FW}, and the mode-averaged transmission probabilities for turning left P_L and turning right P_R, as shown in Eq. (4):

$$R_B^s = \frac{h}{e^2}\frac{P_L P_R - P_{FW}^2}{D} \quad (4a)$$

$$D = (P_L + P_R)[2P_{FW}(P_{FW} + P_L + P_R) + P_L^2 + P_R^2] \quad (4b)$$

For $B = 0$, P_{FW} exceeds both P_L and P_R, and thus, ($P_L P_R$- P_{FW}^2) becomes negative, leading to $R_B^s < 0$. When a magnetic field is introduced, the ballistic electrons are deflected by the Lorentz force, causing a reduction in P_{FW} and an increase in either P_L or P_R, which in turn increases R_B^s. As shown in Fig. 4b, the increase in R_B^s with B is more pronounced in the ballistic regime ($W = 150$ nm) than in the diffusive regime ($W = 1\ \mu m$) because in the ballistic regime, the electron trajectories are more well-defined. The characteristic magnetic field B_0 at which the cyclotron radius $r_c = \hbar k_F/eB$ matches the channel width is

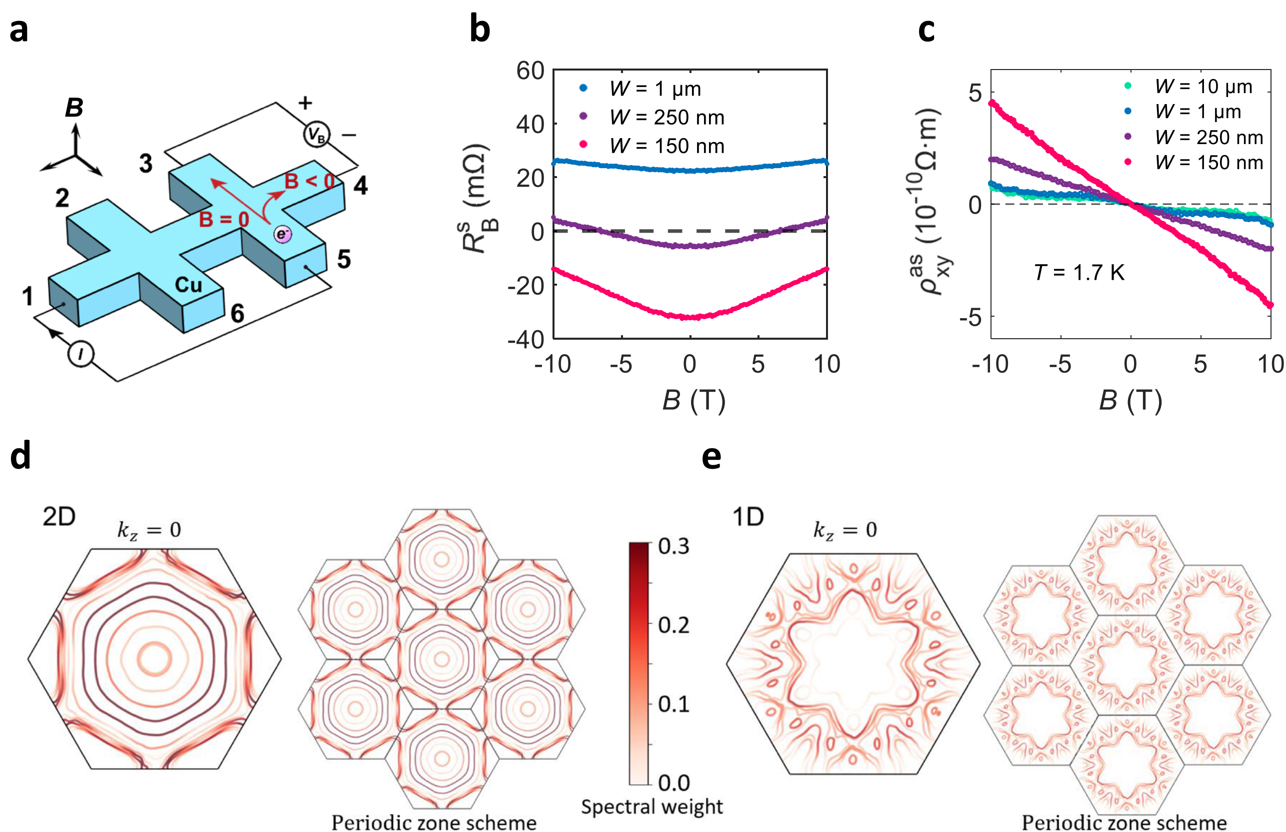

Fig. 4 | Magnetic field dependence of bend resistance and geometrical effect. **a** Measurement schematics for symmetrized bend resistance (R^s_B) in magnetic field (B). **b** B dependence of R^s_B in a single-crystalline Cu(111) thin film (SCCF) Hall bar with widths of $W = 1$ μm, 250 nm, and 150 nm at temperature $T = 4.3$ K. **c** B dependence of antisymmetrized Hall resistivity ρ^{as}_{xy} in the SCCF Hall bar with various W at $T = 1.7$ K. Current was applied from terminal 1 to 4, and Hall voltage was measured between terminals 3 and 5. **d** Calculated effective Fermi surfaces of Cu(111) thin film in the 2D limit at $k_z = 0$. The inner surfaces of 2D limit Fermi surface are split bands due to confined geometry along the out-of-plane direction (left panel). Calculated effective Fermi surfaces of 2D Cu in periodic zone scheme (right panel). 2D effective Fermi surface is obtained by band unfolding to 3D. Color of the band represents the spectral weight of the effective band. **e** Calculated effective Fermi surfaces of 1D Cu(111) at $k_z = 0$ (left panel) and calculated effective Fermi surfaces of 1D Cu in periodic zone scheme (right panel). 1D effective Fermi surface is obtained by band unfolding to 2D.

estimated to be ~36 T for $W = 250$ nm. Here, k_F is the Fermi wavevector of bulk Cu[53], $k_F \approx 1.36 \times 10^{10}$ m^{-1}. Consistent with the expectation for ballistic transport[54], we observe a monotonic increase of R^s_B up to our maximum accessible magnetic field of ~10 T that is smaller than B_0.

To characterize the charge carrier types for devices, we performed Hall measurements and plotted antisymmetrized Hall resistivity ρ^{as}_{xy} for different W at 1.7 K, as shown in Fig. 4c (see Supplementary Fig. 14 for ρ^{as}_{xy} measured at 120 K). The observed nonlinear Hall effect at devices with $W = 10$ and 1 μm agrees with the results of a recent study[45], which revealed the co-existence of holes and electrons in <205-nm-thick SCCFs without GBs. However, when the width is reduced to ≤250 nm, the Hall effect becomes linear, which suggests that electrons become the major charge carriers. To explain this phenomenon in 1D, we calculated and compared effective band structures of a 2D Cu(111) thin film (Fig. 4d) along specific k-points with those of a 1D Cu(111) rod (Fig. 4e). In the 2D thin-film band structure, both electron and hole orbits are distinctly visible. In contrast, the 1D structure's band structure appears more complex due to confined geometry in both out-of-plane and in-plane directions.

The Fermi surface of the 2D thin film shows splitting of degenerate bands due to confined geometry along the [111] direction (Fig. 4d, left panel). In the periodic zone scheme representation (Fig. 4d, right panel), the spectral weight of hole bands is prominent[45]. The 1D structure's Fermi surface is featureless, offering negligible insights. Thus, we calculated the effective Fermi surface via band unfolding to 2D (Fig. 4e, left panel). In the unfolded periodic zone scheme (Fig. 4e, right panel), the spectral density of hole bands is reduced, disconnecting the hole orbits and allowing electron orbits to dominate. Although the calculation system size is smaller than the actual device, it shows the trend of reduced hole orbits as geometry approaches 1D. This explains the experimental observation that the two-carrier model-induced nonlinear Hall effect becomes linear with decreasing W. For reference, Supplementary Fig. 15 compares the 3D, 2D, and 1D Fermi surfaces at a given k_z.

In this study, we observed ballistic electronic transport in nanodevices based on Cu(111) thin films and investigated its dependence on film quality. Hall-bar-shaped devices were fabricated with atomically flat 90-nm-thick SCCFs. We obtained negative bend resistance as direct evidence of ballistic transport. In a perpendicular magnetic field, ballistic electrons are disturbed, increasing bend resistance. We determined the distributions of GBs and TBs through EBSD measurement and showed that the Cu thin-film device's resistivity primarily depended on GBs, remaining insensitive to TBs. Our experimental observations and theoretical calculations reveal that as the Cu(111) thin film transitions from 2D to the 1D limit, hole orbits observed in 2D disappear because of quantum confinement in both out-of-plane and in-plane directions, suggesting transition from nonlinear Hall effect, driven by two carriers, to a linear Hall effect.

This paper presents a platform for investigating the intrinsic quantum mechanical properties of Cu, with the potential to advance high-performance electronic[55] and spintronic devices through preservation of quantum information, including momentum, quantum phase, and spin. This approach may help address critical reliability challenges in semiconductor technology, such as Joule heating[30] and electromigration[31] in

Cu interconnects[29]. Recent discoveries reveal that the Fermi surface of Cu exhibits a topologically nontrivial genus[24], opening the door to various topology-related experiments in ballistic metals[24–26].

Methods

Preparation of thin SCCFs using the ASE technique

The ASE method involves stacking atoms individually without forming clusters, which can cause arbitrary deposition. To achieve this, we modified the conventional sputtering system. The network of conducting wires, including cables, in the conventional sputtering system was upgraded with single-crystalline Cu wires, fabricated by cutting single-crystal Cu wafers in a spiral fashion using wire electrical discharge machining (EDM). The wafers were sliced from a single-crystal ingot grown by the Czochralski method. To minimize vibration from ambient noise, we implemented a mechanical noise reduction system. While such vibrations may not significantly affect conventional thin film growth, especially for PCCFs, they can cause irreversible stacking faults that disrupt the initial nucleation and lateral growth processes, particularly the coherent coplanar merging of nuclei. The thin film growth system creates a stable environment for single-atom deposition, aiming to achieve atomically flat surfaces through precise stacking of single atoms.

The optimized sputtering conditions were as follows:

- Substrate: a double-sided polished (001) Al_2O_3 wafer with a thickness of 430 μm.
- Deposition temperature: approximately 170 °C.
- RF power: 13.56 MHz at 30 W.
- Target-to-substrate distance: 95 mm.
- Base pressure: Maintained at less than 2×10^{-7} Torr.
- Working pressure: 5.4×10^{-3} Torr with an Ar gas (99.9999% (6N)) flow of 50 sccm.

The relationship between the deposition time and thickness of the thin film (or the average growth rate) was determined from the average deposition time of a 200-nm-thick film grown under optimal conditions.

Sample nanofabrication and transport measurement

To fabricate Hall bar devices using the prepared SCCFs, we partially removed sections of single-crystalline Cu via electron beam lithography and Ar-ion milling, forming Hall bars with varying linewidths (Supplementary Fig. 3). After the Ar-ion milling, Cu redeposition was observed along the lithography resist sidewalls (Supplementary Fig. 16), but such regions may have only limited contribution to conduction because they likely exhibit reduced crystallinity. The Cu atomic spacing was 2.07 Å along the (111) direction, confirming that the pristine crystalline quality of the SCCF was maintained even after patterning (Fig. 1b). Temperature dependence of the bend resistance and magnetic field dependence of the Hall resistivity of the SCCF Hall bar devices were measured in Oxford Instruments Teslatron PT with a base temperature of 1.7 K connected with low-pass RC filters. GB dependence of bend resistance, magnetic field dependence of bend resistance, and longitudinal resistance of SCCF Hall bar devices were measured in Oxford Instruments Heliox with a base temperature of 4.3 K, connected with low-pass RC filters. Bend and longitudinal resistance were measured by the DC IV-sweep method by measuring the voltage drop with a Keithley 2000 voltmeter, and the current was applied at 200 nA through Yokogawa GS610 source measure unit with a load resistance of 100 kΩ. Hall resistance was measured using the Delta measurement method by measuring the voltage drop with low-noise Keithley 2182 nanovoltmeter, and current with 1 mA was applied through low-noise Keithley 6221 current source.

Structural information of Hall bar pattern

To investigate the cross-sectional structure of ballistic transport in the SCCF, the annular dark-field (ADF) imaging mode of aberration-corrected scanning transmission electron microscopy (STEM; JEM-ARM200CF, JEOL) at 300 kV was employed. The angle range of the ADF detector was set to 45–175 mrad, and the semiconvergence angle of the condenser lens was ≈24 mrad. In combination with STEM imaging, elemental mapping of the Cu films was performed in the same STEM image mode using electron energy loss spectroscopy (EELS; Quantum ER965, Gatan). Cross-sectional TEM sampling was conducted using the Ga-ion milling and slicing method in a focused-ion-beam scanning electron microscope (SEM; Helios NanoLab 450, Thermo Fisher Scientific). Low-energy Ar-ion beam milling at 700 V for 10 min was sequentially performed as a post-surface treatment to remove the damaged surface layer that usually forms during heavy Ga-ion beam milling.

Theoretical calculations

The total energy and electronic band structure calculations were performed using the first-principles density functional theory[56] as implemented by Kresse and Joubert[57] using the projector augmented-wave method[58]. The exchange–correlation functional was modeled using the generalized gradient approximation in the Perdew–Burke–Ernzerhof form[59]. All the calculations were spin-polarized, and the positions of the atoms, as well as the size and shape of the unit cell, were fully relaxed to obtain the optimized lattice structure. All the atoms of bulk Cu were fully relaxed until the force on the atom was less than 0.001 eV/Å, and the change in total energy was less than 10^{-6} eV. The electron wavefunctions were expanded using a plane-wave basis set with a cut-off energy of 400 eV for the bulk, slab, and rod calculations. A 12-ML (ML: monolayer) Cu(111) slab structure was used to simulate the 2D-limit thin film, and a 6-ML × 6-ML rod structure was used for the 1D-limit nanorod. The choice of a 12-ML Cu(111) slab is supported by thickness-convergence tests on 6-, 9-, and 12-ML slabs (Supplementary Fig. 17). We maintained a 20-Å-thick vacuum layer to prevent interactions between the periodic images.

Data availability

Source data related to the figures in this paper are available in the Figshare repository under https://doi.org/10.6084/m9.figshare.31153522. Additional data are available from the corresponding author upon a reasonable request.

Code availability

The MATLAB scripts used to load the deposited data and reproduce the plots are available in the Figshare repository under https://doi.org/10.6084/m9.figshare.31153522.

References

1. Datta, S. *Electronic Transport in Mesoscopic Systems* (Cambridge University Press, 1997).
2. Kramer, B. Influence of the phase coherence length on ballistic transport. *Z. Phys. B Condens. Matter* **76**, 457 (1989).
3. Heiblum, M. et al. Direct observation of ballistic transport in GaAs. *Phys. Rev. Lett.* **55**, 2200 (1985).
4. Mayorov, A. S. et al. Micrometer-scale ballistic transport in encapsulated graphene at room temperature. *Nano Lett.* **11**, 2396 (2011).
5. Pippard, A. B. *Magnetoresistance in Metals* Vol. 2 (Cambridge University Press, 1989).
6. Ziman, J. M. *The Physics of Metals* (Cambridge University Press, 2011).
7. Abrikosov, A. A. *Fundamentals of the Theory of Metals* (Courier Dover Publications, 2017).
8. Segall, B. Fermi surface and energy bands of copper. *Phys. Rev.* **125**, 109 (1962).
9. Roaf, D. The Fermi surfaces of copper, silver and gold. II. Calculation of the Fermi surfaces. *Philos. Trans. R. Soc. Lond. A Math. Phys. Sci.* **255**, 135 (1962).

10. Zhang, S. et al. Magnetoresistance from Fermi surface topology. *Phys. Rev. B* **99**, 035142 (2019).
11. Takatsu, H. et al. Extremely large magnetoresistance in the non-magnetic metal $PdCoO_2$. *Phys. Rev. Lett.* **111**, 056601 (2013).
12. Kaplan, D. et al. Unification of nonlinear anomalous Hall effect and nonreciprocal magnetoresistance in metals by the quantum geometry. *Phys. Rev. Lett.* **132**, 026301 (2024).
13. Shoenberg, D. The de Haas-van Alphen effect in copper, silver and gold. *Philos. Mag.* **5**, 105 (1960).
14. Fawcett, E. High-field galvanomagnetic properties of metals. *Adv. Phys.* **13**, 139 (1964).
15. Klauder, J. et al. Study of the fine structure in the high-field galvanomagnetic properties and the Fermi Surface of Copper. *Phys. Rev.* **141**, 592 (1966).
16. Courths, R. et al. Photoemission experiments on copper. *Phys. Rep.* **112**, 53 (1984).
17. Kip, A. et al. Cyclotron resonance in copper. *Phys. Rev.* **124**, 359 (1961).
18. Chambers, R. G. The anomalous skin effect. *Proc. R. Soc. Lond. A Math. Phys. Sci.* **215**, 481 (1952).
19. Morse, R. et al. Magnetic oscillations of ultrasonic attenuation in a copper crystal at low temperatures. *Phys. Rev. Lett.* **2**, 250 (1959).
20. Mallikarjunan, A. et al. Resistivity of copper films at thicknesses near the mean free path of electrons in copper minimization of the diffuse scattering in copper. *Electrochem. Solid-State Lett.* **3**, 437 (2000).
21. Kim, S. J. et al. Color of copper/copper oxide. *Adv. Mater.* **33**, 2007345 (2021).
22. Kim, S. J. et al. Flat-surface-assisted and self-regulated oxidation resistance of Cu (111). *Nature* **603**, 434 (2022).
23. Büttiker, M. Four-terminal phase-coherent conductance. *Phys. Rev. Lett.* **57**, 1761 (1986).
24. Kane, C. Quantized nonlinear conductance in ballistic metals. *Phys. Rev. Lett.* **128**, 076801 (2022).
25. Tam, P. M. et al. Probing Fermi sea topology by Andreev state transport. *Phys. Rev. Lett.* **130**, 096301 (2023).
26. Tam, P. M. et al. Topological andreev rectification. *Phys. Rev. B* **107**, 245422 (2023).
27. Van Haesendonck, C. et al. The Aharonov-Bohm effect in normal metals. *Europhys. News* **19**, 89 (1988).
28. Imry, Y. et al. Quantum interference and the Aharonov-Bohm effect. *Sci. Am.* **260**, 56 (1989).
29. Merchant, S. M. et al. Copper interconnects for semiconductor devices. *JOM* **53**, 43 (2001).
30. Chiang, T.-Y. et al. Impact of Joule heating on scaling of deep sub-micron Cu/low-k interconnects. In *Proc. Symposium on VLSI Technology—Digest of Technical Papers* (IEEE, 2002).
31. Zahedmanesh, H. et al. Copper electromigration: prediction of scaling limits. In *Proc. International Interconnect Technology Conference* (IEEE, 2019).
32. van der Pauw, L. J. A method of measuring the resistivity and Hall coefficient on lamellae of arbitrary shape. *Philips Tech. Rev.* **20**, 220 (1958).
33. Ziman, J. *Electrons and Phonons* (Clarendon Press, 1960).
34. Martin, N. et al. Low temperature dependence of resistivity in obliquely sputter-deposited gold thin films. *Surf. Coat. Technol.* **499**, 131884 (2025).
35. Bid, A. et al. Temperature dependence of the resistance of metallic nanowires of diameter$\geqslant$ 15 nm: applicability of Bloch-Grüneisen theorem. *Phys. Rev.* **74**, 035426 (2006).
36. Timalsina, Y. P. et al. Effects of nanoscale surface roughness on the resistivity of ultrathin epitaxial copper films. *Nanotechnology* **26**, 075704 (2015).
37. Shoenberg, D. *Magnetic Oscillations in Metals* (Cambridge University Press, 2009).
38. Kittel, C. et al. *Introduction to Solid State Physics* (John Wiley & Sons, 2018).
39. Goel, N. et al. Ballistic transport in InSb mesoscopic structures. *Phys. E Low Dimens. Syst. Nanostruct.* **26**, 455 (2005).
40. Beenakker, C. et al. Billiard model of a ballistic multiprobe conductor. *Phys. Rev. Lett.* **63**, 1857 (1989).
41. Wu, W. et al. Influence of surface and grain-boundary scattering on the resistivity of copper in reduced dimensions. *Appl. Phys. Lett.* **84**, 2838 (2004).
42. Schwartz, A. J. et al. *Electron Backscatter Diffraction in Materials Science* Vol. 2 (Springer, 2009).
43. Rohrer, G. et al. Deriving grain boundary character distributions and relative grain boundary energies from three-dimensional EBSD data. *Mater. Sci. Technol.* **26**, 661 (2010).
44. Ha, T. et al. Coherent consolidation of trillions of nucleations for mono-atom step-level flat surfaces. *Nat. Commun.* **14**, 685 (2023).
45. Ok, J. M. et al. Hole-carrier-dominant transport in 2D single-crystal copper. *Adv. Mater.* **36**, 2403783 (2024).
46. Lu, L. et al. Ultrahigh strength and high electrical conductivity in copper. *Science* **304**, 422 (2004).
47. Gall, D. The search for the most conductive metal for narrow interconnect lines. *J. Appl. Phys.* **127**, 050901 (2020).
48. Sutton, A. P. *Interfaces in Crystalline Materials* 414 (Oxford University Press, 1995).
49. Kim, T.-H. et al. Structural dependence of grain boundary resistivity in copper nanowires. *Jpn. J. Appl. Phys.* **50**, 08LB09 (2011).
50. Mayadas, A. et al. Electrical-resistivity model for polycrystalline films: the case of arbitrary reflection at external surfaces. *Phys. Rev. B* **1**, 1382 (1970).
51. Fuchs, K. The conductivity of thin metallic films according to the electron theory of metals. *Math. Proc. Camb. Philos. Soc.* **34**, 100–108 (1938).
52. Sondheimer, E. H. The mean free path of electrons in metals. *Adv. Phys.* **50**, 499 (2001).
53. Balcerzak, T. Calculation of the Fermi wave vector for thin films, quantum wires and quantum dots. *Mater. Sci.-Pol.* **24**, 719 (2006).
54. Banszerus, L. et al. Ballistic transport exceeding 28 μm in CVD grown graphene. *Nano Lett.* **16**, 1387 (2016).
55. Kolkowitz, S. et al. Probing Johnson noise and ballistic transport in normal metals with a single-spin qubit. *Science* **347**, 1129 (2015).
56. Kohn, W. et al. Self-consistent equations including exchange and correlation effects. *Phys. Rev.* **140**, A1133 (1965).
57. Kresse, G. et al. From ultrasoft pseudopotentials to the projector augmented-wave method. *Phys. Rev. B* **59**, 1758 (1999).
58. Blöchl, P. E. Projector augmented-wave method. *Phys. Rev. B* **50**, 17953 (1994).
59. Perdew, J. P. et al. Generalized gradient approximation made simple. *Phys. Rev. Lett.* **77**, 3865 (1996).

Acknowledgements

This research was supported by the National Research Foundation of Korea (NRF) (nos. RS-2022-NR068223, RS-2024-00393599, RS-2024-00442710, RS-2024-00444725, RS-2024-00434439, RS-2025-02317602 received by G.-H.L., 2021R1A5A1032937, RS-2024-00406152, and RS-2024-00455226 received by S.-Y.J.), and by the ITRC (Information Technology Research Center) support program (IITP-2025-RS-2022-00164799 received by G.-H.L.). Nanofabrication was partially supported by the POSTECH Center for Semiconductor Technology Convergence, supported by the Korea Basic Science Institute, NFEC-2025-03-304835. G.-H.L. acknowledges the support of Samsung Electronics Co., Ltd (IO201207-07801-01), and S.-Y.J. acknowledges the support of Samsung Science and Technology Foundation (project number SRFC-MA2202-02).

Author contributions

G.-H.L., S.-Y.J., H.-J.L., and S.-G.K. conceived this study. Y.J.C. performed the transport measurements. S.-Y.J., S.J.K., and Y.L. performed the Cu thin film growth and observation using AFM, XRD, EBSD, and SEM. M.-H.J., H.Y.J., and Y.-M.K. performed TEM measurements and analyses. S.-G.K. and H.-J.L. supervised the work. G.-H.L., S.-Y.J., S.-G.K., and Y.J.C. wrote the manuscript. All authors participated in the manuscript review.

Competing interests

The authors declare no competing interests.

Additional information

Supplementary information The online version contains supplementary material available at https://doi.org/10.1038/s41467-026-70252-2.

Correspondence and requests for materials should be addressed to Seong-Gon Kim, Se-Young Jeong or Gil-Ho Lee.

Peer review information *Nature Communications* thanks Pascal Gehring and the other, anonymous, reviewer(s) for their contribution to the peer review of this work. A peer review file is available.

Reprints and permissions information is available at http://www.nature.com/reprints

Publisher's note Springer Nature remains neutral with regard to jurisdictional claims in published maps and institutional affiliations.

Open Access This article is licensed under a Creative Commons Attribution-NonCommercial-NoDerivatives 4.0 International License, which permits any non-commercial use, sharing, distribution and reproduction in any medium or format, as long as you give appropriate credit to the original author(s) and the source, provide a link to the Creative Commons licence, and indicate if you modified the licensed material. You do not have permission under this licence to share adapted material derived from this article or parts of it. The images or other third party material in this article are included in the article's Creative Commons licence, unless indicated otherwise in a credit line to the material. If material is not included in the article's Creative Commons licence and your intended use is not permitted by statutory regulation or exceeds the permitted use, you will need to obtain permission directly from the copyright holder. To view a copy of this licence, visit http://creativecommons.org/licenses/by-nc-nd/4.0/.

© The Author(s) 2026